Author/s:
Liu, W;Tian, Y;Cassidy, MJ

Title:
An interface to numerically model undrained soil-structure interactions

Date:
2021-10-01

Citation:
Liu, W., Tian, Y. & Cassidy, M. J. (2021). An interface to numerically model undrained soil-structure interactions. Computers and Geotechnics, 138, https://doi.org/10.1016/j.compgeo.2021.104327.

Persistent Link:
https://hdl.handle.net/11343/302872

Computers and Geotechnics 138 (2021) 104327

Contents lists available at ScienceDirect

Computers and Geotechnics

journal homepage: www.elsevier.com/locate/compgeo

An interface to numerically model undrained soil-structure interactions

Wenlong Liu, Yinghui Tian *, Mark J. Cassidy

Department of Infrastructure Engineering, Faculty of Engineering and Information Technology, The University of Melbourne, Parkville, Victoria 3010, Australia

ARTICLE INFO

Keywords:
Interface model
Soil-structure interaction
Interface roughness
Undrained behaviour
Integration algorithm

ABSTRACT

The traditional Coulomb friction model is commonly used to illustrate interactions at the soil-structure interface, but it assumes zero tangential resistance when the normal stress on the interface is in tension. This is not realistic for modelling the undrained behaviour of geo-structures deeply embedded in the seabed because the soil adheres to the structure due to the suction generated. This note proposes a new interface model that captures the undrained behaviour of soil at the structural interface, including the ability to maintain frictional shear stresses under tensile normal stress. Based on simple elastic-perfectly plasticity theory the constitutive behaviour of the interface and the algorithm required to numerically implement it into a finite element program are fully described. Computational cases are presented to verify the model's implementation and demonstrate how the new interface model performs for cases of undrained behaviour encountered in offshore geotechnics.

1. Introduction

In offshore geotechnical engineering, undrained soil behaviour commonly occurs in low permeability clay seabeds when the loading process is short and pore-pressures do not have time to dissipate. Examples include penetrometers, such as T-bars (e.g. Randolph and Andersen, 2006), that are pushed vertically into the seabed to derive the soil's strength, and the installation and operational loading of footings (e.g. Gourvenec et al., 2006), spudcans (e.g. Hossain et al., 2006), pipelines (e.g. Hodder et al., 2008) and anchors (e.g. O'Neill et al., 2003). In these scenarios the soil at the front face of the advancing direction is in compression while the rear face is in tension with transient suction generated in the soil (Dingle et al., 2008; Zhou et al., 2018).

Modelling these problems within the finite element method requires a soil-structure interface that can account for both the normal and tangential behaviour between the soil and structure on all contacting faces. Most available soil-structure interfaces adopt a pressure-overclosure relationship formulated with a penalty stiffness to describe the normal behaviour (Qiu et al., 2011; Zhou et al., 2018). When the normal pressure reduces to zero, separation is allowed. These are usually referred to as 'zero-tension' interfaces (Shen et al., 2016). For deeply embedded structures in undrained conditions, the soil-structure interface is not expected to separate due to the generated suction (O'Neill et al., 2003; Zhou and Randolph, 2007). In this scenario, interfaces need to be formulated to sustain the tension between the contacting surfaces. As one example, Zhou et al. (2018) defined an interface where the tension is maintained before the gap between the contacting surfaces exceeds a tolerance.

As for the tangential behaviour, a maximum tangential shear strength $\tau_{\max}$ between the structure and soil is often defined as a portion of the undrained strength s_u of the soil

$$\tau_{max} = \alpha s_u \tag{1}$$

where α can be considered the interface roughness. In finite element software, such as ABAQUS, a 'fully bonded' condition can be realised using 'Rough' contact (with no separation allowed) or 'Tie' constraint to couple the contacting nodes (see Dassault Systèmes, 2014). This essentially means $\alpha = \infty$ because the relative sliding of two contacting surfaces is not allowed, and infinite shear resistance is modelled along the contacting surfaces.

A more commonly used method is the traditional Coulomb friction model, in which a finite roughness α is specified. Fig. 1 illustrates the Coulomb friction model showing the relationship between critical tangential resistance τ_{crit} (when sliding starts) and normal pressure p. The critical tangential resistance τ_{crit} is linearly related to the normal pressure p through a friction factor μ before reaching the stabilised maximum shear resistance $\tau_{\max}$, which is related to the soil strength, as shown in Eq. (1). $\alpha = 1$ is in fact not exactly the same as the fully bonded condition (with $\alpha = \infty$), although these two scenarios may give comparable results in numerical modelling and thus have been commonly used interchangeably (as shown in Merifield et al., 2008; Wang et al.,

* Corresponding author.
E-mail addresses: wenlong@student.unimelb.edu.au (W. Liu), yinghui.tian@unimelb.edu.au (Y. Tian), mark.cassidy@unimelb.edu.au (M.J. Cassidy).

https://doi.org/10.1016/j.compgeo.2021.104327
Received 21 May 2021; Received in revised form 18 June 2021; Accepted 25 June 2021
Available online 14 July 2021

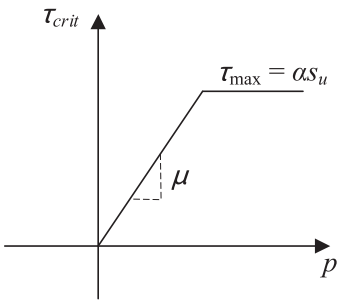

Fig. 1. Coulomb friction model.

2017), especially when the objects in contact are simple geometries. As shown later in this note, $\alpha = 1$ may predict a lower soil resistance for complicated geometries compared with the fully bonded interface ($\alpha = \infty$).

Moreover, when the normal stress is in tension, the Coulomb friction model predicts zero tangential resistance. This is not realistic for undrained behaviour in deeply embedded cases because the generated suction in the soil can hold the contacting faces together, and thus the tangential resistance still exists. Therefore, adoption of the traditional Coulomb friction model in this scenario tends to underestimate the soil resistance (Ramirez et al., 2014; Wang et al., 2017). This can be significant for deeply embedded penetrometers and foundations, as shown later in this note.

The present technical note addresses this problem by developing a new interface to reasonably account for the tangential stress between the soil and structure under tension to enable modelling of undrained behaviour of soil-structure interactions. The interface model is described within the elastic-perfectly plasticity framework and a detailed integration algorithm is provided for easy implementation in finite element programs (for instance the ABAQUS user subroutine FRIC was used in this note). The interface model was validated, and its performance was demonstrated, by presenting computational results of example cases from offshore engineering practice.

2. Description of the interface model

This three-dimensional interface model has two orthogonal components of shear stresses denoted as τ_1 and τ_2 and one normal stress σ_n, as shown in Fig. 2. The normal contact behaviour is defined by a pressure-overclosure relationship with a large penalty stiffness. The formulation in this note allows the interface to sustain the tension between the contacting surfaces.

The tangential behaviour is based on an elastic-perfectly plastic constitutive relationship, comprising a yield surface, elastic behaviour within the yield surface and a flow rule. The yield surface function of the shear stress τ_1 and τ_2, as illustrated in Fig. 3, can be written as:

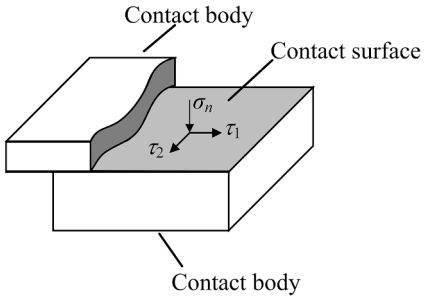

Fig. 2. Normal and tangential stress components on the contact surface.

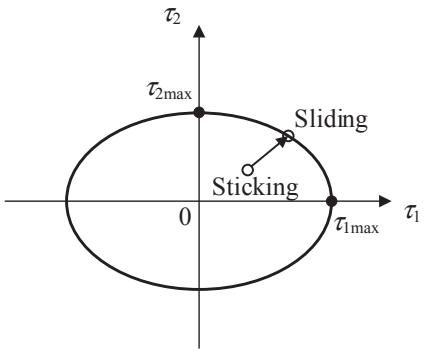

Fig. 3. Yield surface.

$$f = \left(\frac{\tau_1}{\tau_{1max}}\right)^2 + \left(\frac{\tau_2}{\tau_{2max}}\right)^2 - 1 = 0 \tag{2}$$

where $\tau_{1\max}$ and $\tau_{2\max}$ are the allowable shear strengths along the orthogonal 1 and 2 directions, respectively.

Elastic shear displacement occurs for increments of shear stress within the yield surface, also termed as 'sticking' state (Amaireh and Haikal, 2018). Sliding occurs when the shear stress is on the yield surface. Consequently, the shear displacement increment $d\mathbf{U}$ can be decomposed into an elastic (i.e. reversible sticking) increment $d\mathbf{U}^e$ and a plastic (i.e. irreversible slip) increment $d\mathbf{U}^p$ (Amaireh and Haikal, 2018)

$$d\mathbf{U} = d\mathbf{U}^e + d\mathbf{U}^p \tag{3}$$

For shear stress inside the yield surface, the elastic response is

$$d\boldsymbol{\tau} = \begin{Bmatrix} d\tau_1 \\ d\tau_2 \end{Bmatrix} = \mathbf{D}^e d\mathbf{U}^e = \begin{bmatrix} k_1 & 0 \\ 0 & k_2 \end{bmatrix} \begin{Bmatrix} d\gamma_1^e \\ d\gamma_2^e \end{Bmatrix} \tag{4}$$

where $d\boldsymbol{\tau}$ is the shear stress increment vector, $d\mathbf{U}^e = \{d\gamma_1{}^e, d\gamma_2{}^e\}^{\mathrm{T}}$ is the elastic displacement increment vector, $\mathbf{D}^e$ is the elastic stiffness matrix and k_1 and k_2 are the elastic stiffnesses along two local orthogonal directions. As illustrated in Fig. 4, the elastic stiffness can be described

$$k_1 = \frac{\tau_{1max}}{\gamma_{1crit}}, \quad k_2 = \frac{\tau_{2max}}{\gamma_{2crit}} \tag{5}$$

where γ_{1crit} or γ_{2crit} is the maximum allowable elastic 'sticking' along the two local orthogonal directions. In this note, γ_{1crit} and γ_{2crit} were adopted as 0.005 that of the contacting element length. This provided realistic modelling results and stable numerical convergence for the practical examples demonstrated later in this note.

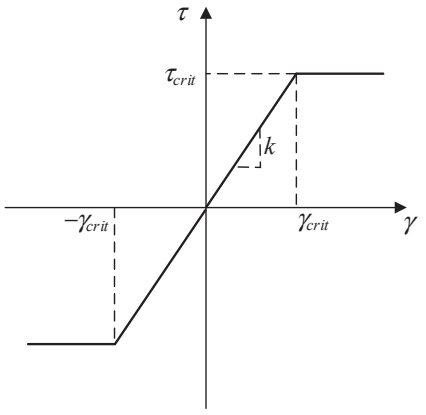

Fig. 4. Allowable elastic displacement for modelling Coulomb friction.

The interface model adopts an associated flow rule, allowing the plastic potential function g to be defined simply as f. Thus, the plastic slip increment $d\mathbf{U}^p$ is expressed by

$$d\mathbf{U}^p = d\lambda\frac{\partial g}{\partial \boldsymbol{\tau}} = d\lambda\frac{\partial f}{\partial \boldsymbol{\tau}} = d\lambda\begin{Bmatrix}\dfrac{\partial f}{\partial \tau_1}\\ \dfrac{\partial f}{\partial \tau_2}\end{Bmatrix} = \begin{Bmatrix}\dfrac{2d\lambda\tau_1}{\tau_{1max}^2}\\ \dfrac{2d\lambda\tau_2}{\tau_{2max}^2}\end{Bmatrix} \tag{6}$$

where $\partial g/\partial\boldsymbol{\tau}$ is the gradient vector of the plastic potential function and $d\lambda$ is the plastic multiplier. In terms of Eqs. (3) and (6) and the consistency condition $df = 0$, $d\lambda$ is derived as:

$$d\lambda = \frac{\frac{\partial f}{\partial \boldsymbol{\tau}}^T\mathbf{D}^e d\mathbf{U}}{\frac{\partial f}{\partial \boldsymbol{\tau}}^T\mathbf{D}^e\frac{\partial g}{\partial \boldsymbol{\tau}}} = \frac{\tau_{1max}^2\tau_{2max}^2\left(k_1\tau_1 d\gamma_1\tau_{2max}^2 + k_2\tau_2 d\gamma_2\tau_{1max}^2\right)}{2\left(k_1\tau_1^2\tau_{2max}^4 + k_2\tau_2^2\tau_{1max}^4\right)} \tag{7}$$

The constitutive tangential behaviour, with the elastoplastic stiffness matrix $\mathbf{D}^{ep}$, is:

$$d\boldsymbol{\tau} = \mathbf{D}^e(d\mathbf{U} - d\mathbf{U}^p) = \mathbf{D}^{ep}d\mathbf{U} = \left(\mathbf{D}^e - \frac{\mathbf{D}^e\frac{\partial g}{\partial \boldsymbol{\tau}}\frac{\partial f}{\partial \boldsymbol{\tau}}^T\mathbf{D}^e}{\frac{\partial f}{\partial \boldsymbol{\tau}}^T\mathbf{D}^e\frac{\partial g}{\partial \boldsymbol{\tau}}}\right)d\mathbf{U}$$

$$= \frac{k_1k_2}{k_1\tau_1^2\tau_{2max}^4 + k_2\tau_2^2\tau_{1max}^4}\begin{bmatrix}\tau_2^2\tau_{1max}^4 & -\tau_1\tau_2\tau_{1max}^2\tau_{2max}^2\\ -\tau_1\tau_2\tau_{1max}^2\tau_{2max}^2 & \tau_1^2\tau_{2max}^4\end{bmatrix}\begin{Bmatrix}d\gamma_1\\ d\gamma_2\end{Bmatrix} \tag{8}$$

3. Constitutive integration algorithm for implementation of the interface model

The proposed interface model has been implemented in the finite element software ABAQUS through the user subroutine FRIC (Dassault Systèmes, 2014). During the incremental analysis process, the shear stress $\boldsymbol{\tau}_n$ at time t_n and displacement increment $\Delta\mathbf{U}_{n+1}$ from the n^{th} to $(n+1)^{th}$ increment are provided, while the shear stress $\boldsymbol{\tau}_{n+1} = \{\tau_{1,\,n+1},\, \tau_{2,\,n+1}\}^T$ at the end of the n^{th} increment needs to be defined in FRIC.

Following the explicit algorithm in Tian and Cassidy (2010), trial shear stress $\boldsymbol{\tau}_{n+1}{}^{trial}$ at time t_{n+1} is calculated by assuming full elastic behaviour for $\Delta\mathbf{U}_{n+1}$.

$$\boldsymbol{\tau}_{n+1}^{trial} = \boldsymbol{\tau}_n + \Delta\boldsymbol{\tau}_{n+1}^e = \boldsymbol{\tau}_n + \mathbf{D}^e\Delta\mathbf{U}_{n+1} \tag{9}$$

There are six possible circumstances based on the current shear stress $\boldsymbol{\tau}_n$ and trial shear stress $\boldsymbol{\tau}_{n+1}{}^{trial}$, which are illustrated in Fig. 5. The current stress state $\boldsymbol{\tau}_n$ at t_n is illustrated as a circular point, which can be either within the yield surface (Circumstances 1, 2 and 4) or on the surface (Circumstances 3, 5 and 6). The trial point of Circumstance 1 is just on the yield surface, while Circumstance 2 is within the surface. Circumstance 3 retreats back into the yield surface. No plastic behaviour is involved in these 3 circumstances. Therefore, the trial stress state is accepted as the real stress, i.e., $\boldsymbol{\tau}_{n+1} = \boldsymbol{\tau}_{n+1}{}^{trial}$. For Circumstances 4, 5, and 6, the trial shear stress state is located outside the yield surface, elastoplastic behaviour occurs, and constitutive Eq. (8) requires integration over the displacement increment $\Delta\mathbf{U}_{n+1}$. The shear stress increment $\Delta\boldsymbol{\tau}_{n+1}$ can be integrated as

$$\Delta\boldsymbol{\tau}_{n+1} = \int_{\mathbf{U}_n}^{\mathbf{U}_{n+1}}\mathbf{D}^e(d\mathbf{U} - d\mathbf{U}^p) = \int_{\mathbf{U}_n}^{\mathbf{U}_{n+1}}\mathbf{D}^e\left(d\mathbf{U} - d\lambda\frac{\partial g}{\partial \boldsymbol{\tau}}\right) \tag{10}$$

For Circumstances 4 and 5, the ratio of the pure elastic displacement to the total displacement increment, e, can be calculated to determine the starting point for plasticity integration. By solving the equation $f(\boldsymbol{\tau}_n + e\Delta\boldsymbol{\tau}_{n+1}{}^e) = 0$, the analytical expression of e for isotropic soil material can be obtained as

$$e = \frac{-\tau_{1,n}\Delta\tau_{1,n+1}^e - \tau_{2,n}\Delta\tau_{2,n+1}^e + \sqrt{\tau_{max}^2\left[\left(\Delta\tau_{1,n+1}^e\right)^2 + \left(\Delta\tau_{2,n+1}^e\right)^2\right] - \left(\tau_{2,n}\Delta\tau_{1,n+1}^e - \tau_{1,n}\Delta\tau_{2,n+1}^e\right)^2}}{\left(\Delta\tau_{1,n+1}^e\right)^2 + \left(\Delta\tau_{2,n+1}^e\right)^2} \tag{11}$$

Hence, the displacement increment $\Delta\mathbf{U}_{n+1}$ is divided into two parts, $e\Delta\mathbf{U}_{n+1}$ and $(1-e)\Delta\mathbf{U}_{n+1}$, where $e\Delta\mathbf{U}_{n+1}$ accounts for the pure elastic response and $(1-e)\Delta\mathbf{U}_{n+1}$ accounts for the elastoplastic response. Eq. (10) can be expressed as

$$\Delta\boldsymbol{\tau}_{n+1} = \int_{\mathbf{U}_n}^{\mathbf{U}_n+e\Delta\mathbf{U}_{n+1}}\mathbf{D}^e d\mathbf{U} + \int_{\mathbf{U}_n+e\Delta\mathbf{U}_{n+1}}^{\mathbf{U}_{n+1}}\mathbf{D}^e\left(d\mathbf{U} - d\lambda\frac{\partial g}{\partial \boldsymbol{\tau}}\right)$$

$$= e\Delta\boldsymbol{\tau}_{n+1}^e + \int_{\mathbf{U}_n+e\Delta\mathbf{U}_{n+1}}^{\mathbf{U}_{n+1}}\mathbf{D}^e\left(d\mathbf{U} - d\lambda\frac{\partial g}{\partial \boldsymbol{\tau}}\right) \tag{12}$$

Both Circumstances 5 and 6 satisfy $f(\boldsymbol{\tau}_n) = 0$ and $f(\boldsymbol{\tau}_{n+1}{}^{trial}) > 0$. Circumstance 6 can be distinguished from Circumstance 5 by using a loading criterion:

$$L = \frac{\partial f}{\partial \boldsymbol{\tau}_n}^T\Delta\boldsymbol{\tau}_{n+1}^{trial} \tag{13}$$

Circumstance 5 has $L < 0$ and will experience an unloading process. Circumstance 6 has $L > 0$ with $e = 0$.

This note employed the explicit standard Euler algorithm to solve integration Eq. (10) (see Tian and Cassidy, 2010, for a detailed comparison of a range of implicit and explicit integration algorithms). In the standard Euler algorithm, the displacement increment $(1-e)\Delta\mathbf{U}_{n+1}$ is divided into N subincrements, and the stress subincrements are explicitly calculated based on the stress state at the beginning of each subincrement.

The numerical truncation error during the process of explicit integration may result in the drifting of the integration result $\boldsymbol{\tau}_{n+1}$ from the yield surface. A correction can be achieved by projecting the stress $\boldsymbol{\tau}_{n+1}$ back to the yield surface along the normal direction, which is expressed by

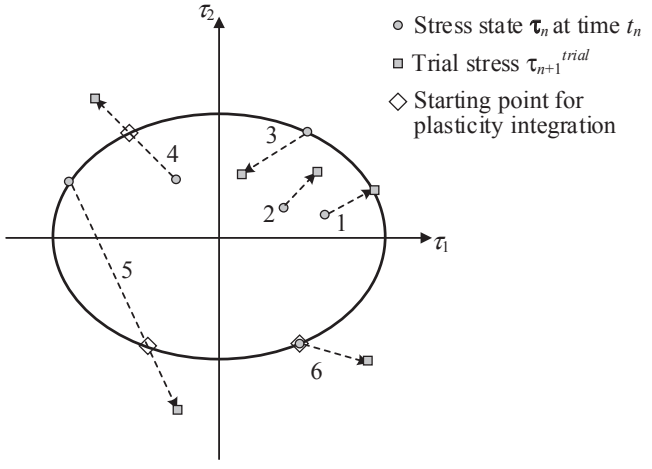

Fig. 5. Possible circumstances of frictional stress state.

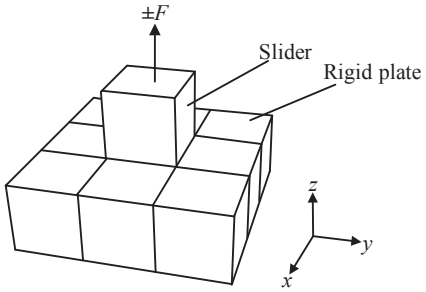

Fig. 6. Finite element model for validation of new interface model.

$$\boldsymbol{\tau}_{n+1} = \boldsymbol{\tau}_{n+1} + \beta\frac{\partial f}{\partial \boldsymbol{\tau}_{n+1}} = \boldsymbol{\tau}_{n+1} - \frac{f(\boldsymbol{\tau}_{n+1})}{\frac{\partial f}{\partial \boldsymbol{\tau}_{n+1}}^{T}\frac{\partial f}{\partial \boldsymbol{\tau}_{n+1}}}\frac{\partial f}{\partial \boldsymbol{\tau}_{n+1}} \tag{14}$$

where β can be derived by solving $f(\boldsymbol{\tau}_{n+1} + \beta \bullet \partial f/\partial \boldsymbol{\tau}_{n+1}) = 0$.

The detailed procedure for shear stress computation is summarised as follows:

(1) Compute the trial stress

$$\boldsymbol{\tau}_{n+1}^{trial} = \boldsymbol{\tau}_n + \Delta\boldsymbol{\tau}_{n+1}^{e} = \boldsymbol{\tau}_n + \mathbf{D}^e\Delta\mathbf{U}_{n+1}$$

(2) Determine the loading state

If $f(\boldsymbol{\tau}_{n+1}{}^{trial}) \le 0$, the trial loading state is in an elastic state or just arrives on the yield surface without plastic behaviour. $\boldsymbol{\tau} \leftarrow \boldsymbol{\tau}_{n+1}{}^{trial}$ and $\mathbf{D} \leftarrow \mathbf{D}^e$ and go to (8).

If $f(\boldsymbol{\tau}_{n+1}{}^{trial}) > 0$, the loading state is in an elastoplastic state. If $f(\boldsymbol{\tau}_n) < 0$, solve e. If $f(\boldsymbol{\tau}_n) = 0$ and $L < 0$, solve e. If $f(\boldsymbol{\tau}_n) = 0$ and $L \ge 0$, $e \leftarrow 0$.

(3) Determine the start point for plasticity integration

$$\boldsymbol{\tau} \leftarrow \boldsymbol{\tau}_n + e\Delta\boldsymbol{\tau}_{n+1}^{e}$$

(4) Dividing $(1 - e)\Delta\mathbf{U}_{n+1}$ into N sub-increments

$$d\mathbf{U} = (1 - e)\Delta\mathbf{U}_{n+1}/N$$

(5) Integrate numerically, loop from $i = 1$ to N

$$d\lambda = \frac{\frac{\partial f}{\partial \boldsymbol{\tau}}^{T}\mathbf{D}^e d\mathbf{U}^{(i)}}{\frac{\partial f}{\partial \boldsymbol{\tau}}^{T}\mathbf{D}^e\frac{\partial g}{\partial \boldsymbol{\tau}}}$$

$$d\boldsymbol{\tau}^{(i)} = \mathbf{D}^e\left(d\mathbf{U}^{(i)} - d\lambda\frac{\partial g}{\partial \boldsymbol{\tau}}\right)$$

$$\boldsymbol{\tau} \leftarrow \boldsymbol{\tau} + d\boldsymbol{\tau}^{(i)}$$

(6) Check the integrated stress

If $|f(\boldsymbol{\tau})| > Tol$,

$$\boldsymbol{\tau} \leftarrow \boldsymbol{\tau} + \beta\frac{\partial f}{\partial \boldsymbol{\tau}}$$

(7) Calculate the stiffness matrix

$$\mathbf{D} \leftarrow \mathbf{D}^{ep}$$

(8) Accept the stress state and stiffness matrix

$$\boldsymbol{\tau}_{n+1} \leftarrow \boldsymbol{\tau},\ \mathbf{D}_{n+1} \leftarrow \mathbf{D}$$

In this study, the number of subincrements N was taken as 1000.

4. Computational analysis cases

Three computational analysis cases are described. The first validates the new interface model by modelling a simple slider on a rigid base. The latter two cases demonstrate the applicability of the new interface model for practical offshore geotechnical modelling problems, initially for simple and then complex geometry.

To mimic undrained conditions in the total stress analysis, infinite tension describes the normal contact behaviour between the contacting surfaces. The shear stress limit was specified as a portion of shear strength s_u, i.e., $\tau_{\max} = \alpha s_u$. The new interface model is compared with the traditional Coulomb friction model built into ABAQUS (see Dassault Systèmes, 2014), which predicts zero shear resistance when the contacting faces are in tension. The three cases assume an isotropic soil material and interface, and thus the allowable shear strength $\tau_{1\max}$ and $\tau_{2\max}$, elastic displacement γ_{1crit} and γ_{2crit}, and elastic stiffness k_1 and k_2 are equal.

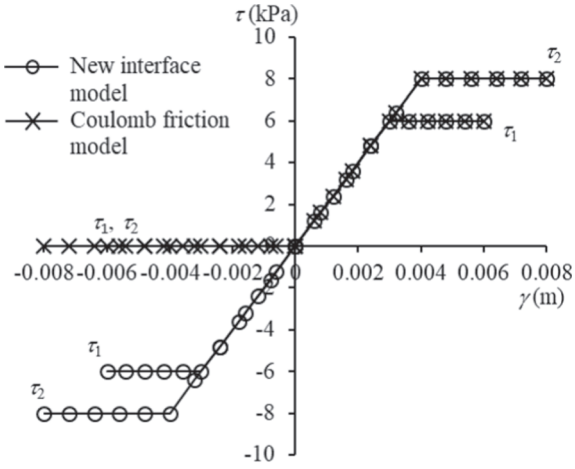

(a) shear stress

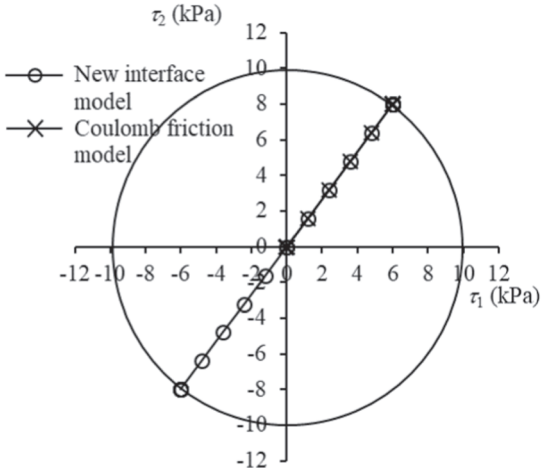

(b) shear stress path

Fig. 7. Comparison of the new interface model and Coulomb friction model. (a) shear stress (b) shear stress path.

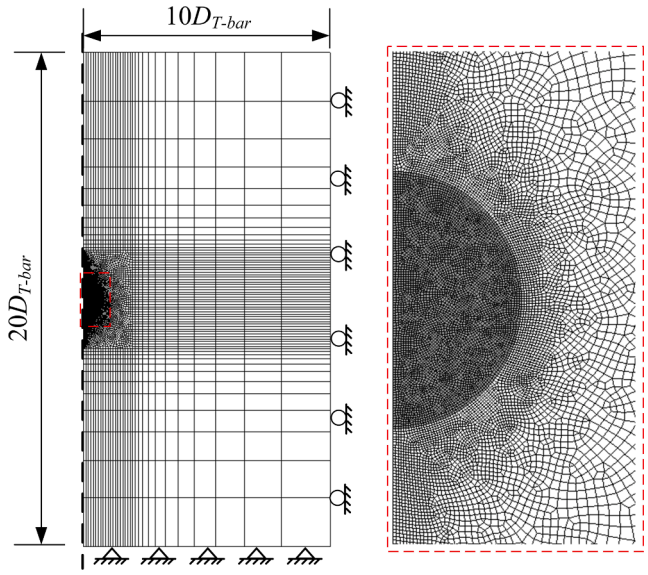

Fig. 8. Finite-element mesh of the T-bar model.

4.1. Case 1: A slider on a rigid plate

The finite element model that consists of a single element slider and nine element rigid base is shown in Fig. 6. Each element has an area of 1 m^2. Surface-to-surface contact was adopted between the bottom of the slider and the top face of the rigid base. For tangential behaviour, the maximum shear strength τ_{max} was 10 kPa and the allowable elastic 'sticking' displacement γ_{crit} was 5 mm (0.005 times the element size). This made the elastic stiffness $k = \tau_{max}/\gamma_{crit} = 2000$ kPa/m.

Two calculation scenarios were considered: (1) a normal compression load $F = 200$ kN was applied on the slider, and then it was displaced 0.01 m with an angle of 53.13° to the x-axis (i.e. 0.006 m and 0.008 m along the x- and y-axes, respectively); (2) a normal tension load $F = -200$ kN was applied on the slider, which was again displaced 0.01 m but in the opposite direction (i.e. −0.006 m and −0.008 m along the x- and y-axes, respectively, noting that the reverse displacement was only to provide a clearer comparison of results when plotted in Fig. 7).

Fig. 7(a) shows the relationship between shear stress and displacement, and Fig. 7(b) shows the corresponding shear stress path for the two scenarios. In Scenario 1, where the normal load is in compression, both the Coulomb friction model in ABAQUS and the interface model

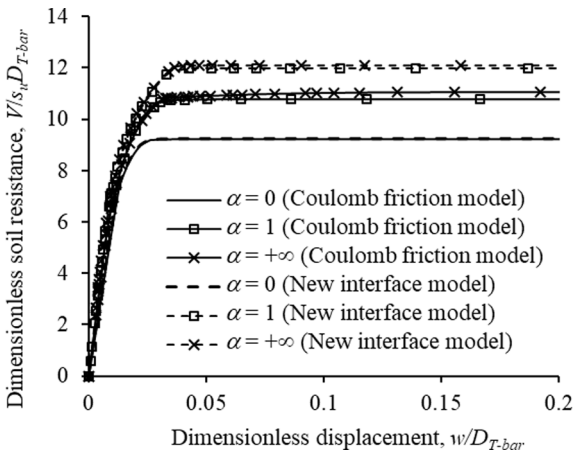

Fig. 9. Resistance response of the T-bar from two interface models.

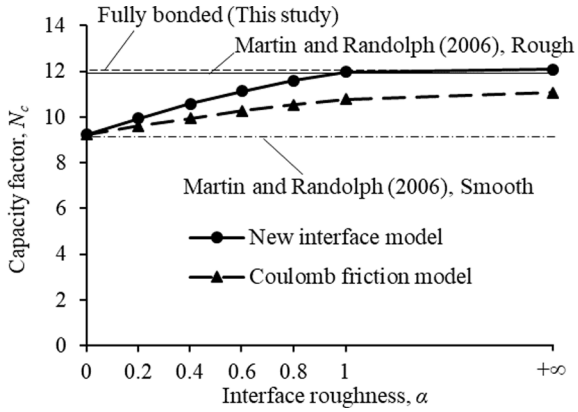

Fig. 10. Effect of interface roughness on the capacity factor of the T-bar.

proposed in this note predict the same results. As expected, the shear stresses τ_1 and τ_2 reached 6 kPa and 8 kPa, respectively, and at the correct shear strains. In Scenario 2, where the normal load is in tension, the interface model in this note predicted that the shear stresses τ_1 and τ_2 reach −6 kPa and −8 kPa (negative values mean the slider has negative tangential displacement), while the shear stress remained at 0 for the Coulomb friction model. Thus, the new interface model realises undrained shear behaviour modelling when the contacting faces are in tension, as expected.

4.2. Case 2: T-bar penetration

A T-bar is a cylindrical full-flow penetrometer used in offshore site investigations to obtain strength profiles of soft sediments (DeJong et al., 2011). Its advantages over the conventional penetrometers (e.g. CPT) are the improved accuracy of assessing the shear strength especially in soft sediments and the minimised corrections for overburden stress (DeJong et al., 2011). Undrained shear strength can be estimated by simply dividing the penetration resistance with a capacity factor N_c, which was rigorously derived from plasticity limit analysis (Randolph and Houlsby, 1984; Martin and Randolph, 2006). Martin and Randolph (2006) derived N_c are 9.2 and 11.94 for $\alpha = 0$ and 1 in the deep mechanism. This computational analysis case investigates the effect of roughness α on the capacity factor N_c of a deep embedded T-bar and compares the new interface model with the Coulomb friction model.

Taking advantage of symmetry, a half model was used, as shown in Fig. 8. The minimum size of soil elements close to the T-bar is $0.01D_{T\text{-}bar}$, where $D_{T\text{-}bar}$, the diameter of the T-bar, is 0.04 m. The horizontal degree of freedom is constrained for the right side of the soil domain. The symmetry condition is imposed on the left side of the soil domain. All degrees of freedom are constrained for the bottom side of the soil domain. The T-bar is displaced vertically by 0.008 m, i.e., $0.2D_{T\text{-}bar}$. In this computation case (and the following Case 3), the soil's material behaviour is modelled as an elastic-perfectly plastic Tresca model with an undrained shear strength of $s_u = 50$ kPa. The soil's elastic behaviour is modelled with Young's modulus $E = 500s_u$ and a Poisson's ratio $\nu = 0.49$. The structure is modelled as a rigid body.

Seven roughness, $\alpha = 0$, 0.2, 0.4, 0.6, 0.8, 1 and 10^6, were considered for both the new interface model and the Coulomb friction model. The latter 10^6 is an arbitrary large number representing infinite roughness. In addition to both the Coulomb model and proposed interface of this note, another calculation case was conducted with a fully bonded interface using the 'Tie' constraint. Thus, a total of 15 calculation cases were conducted. Fig. 9 shows the dimensionless soil resistance $V/s_uD_{T\text{-}bar}$ to the T-bar for selected calculations of $\alpha = 0$, 1 and 10^6. The soil resistance increases to stabilised values with the movement of the T-bar. The stabilised value of the soil resistance V_{max} can be expressed as the

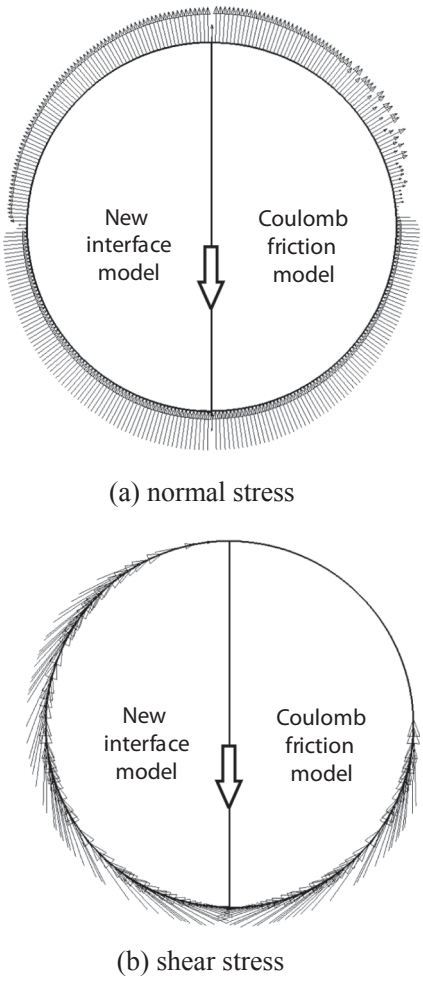

Fig. 11. Normal stress and shear stress of the deeply embedded T-bar ($\alpha = 1$). (a) normal stress (b) shear stress.

dimensionless capacity factor $N_c = V_{max}/s_u D_{T\text{-}bar}$.

Fig. 10 summarises the capacity factor for all the calculations. For $\alpha = 0$ (the smooth interface), the capacity factor is obtained as $N_c = 9.23$ for both the new and Coulomb friction models, which agrees with the theoretical solution of 9.2. When $\alpha > 0$, the new interface model results are higher than those of the Coulomb friction model. For $\alpha = 10^6$, the capacity factor calculated with the new interface model is 12.09, which is the same as the fully bonded interface using the 'Tie' constraint, and within 1.3% of the analytical solution of 11.94. Comparatively, the Coulomb friction model does not approach the analytical solution, with only 11.06 calculated with $\alpha = 10^6$. The reason that the Coulomb friction model failed to give an accurate result is because it only defines the friction on the advancing half of the T-bar and ignores friction on the trailing half where the normal force is in tension, while the new interface model can fulfill the functionality.

Fig. 11 shows the distribution of the normal stress and interface shear stress around the T-bar for $\alpha = 1$. The left half of the T-bar in Fig. 11 is the new interface model proposed in this note, while the right half is the Coulomb friction model. The advancing side of the T-bar (bottom as the T-bar is penetrating the soil) is in compression, and the trailing side (above) is in tension. The Coulomb friction model gives zero shear stress on the trailing side of the T-bar. This is not believed to be realistic for undrained behaviour. On-the-other-hand, Fig. 11 shows shear stresses derived on both advancing and trailing sides of the T-bar by the new interface model and this represents a more appropriate prediction of undrained behaviour in this circumstance.

4.3. Case 3: Mooring chain of anchoring system

The chain is a key part of offshore mooring systems (Yen and Tofani, 1984; Neubecker and Randolph, 1995). Chain segments embedded in the seabed not only connect vessels/platforms to the anchor, but also provide mooring resistance within the chain itself. This calculation case studies the resistance of deeply embedded chain links, which are complex in geometry, using three-dimensional finite element modelling. Again, the focus is on comparing the new interface to the traditional Coulomb model.

As shown in Fig. 12, a finite element model was established to simulate a studless chain link embedded in the soil. The length L of the link is $6d_{chain}$, where d_{chain} is the chain bar's diameter (following DNV GL, 2015; ABS, 2017). One whole link and two half links were used by taking advantage of the cyclic symmetry of a long chain in soil. The centre and two half chain links were modelled as three independent rigid bodies, which allowed the soil resistances on the middle chain link to be extracted. All the chain links were moved together with the same displacement and relative movements among chain links were not permitted. A 'multi-point constraints' (MPC) technique (Dassault Systèmes, 2014) was used to realise the soil's cyclic symmetry by

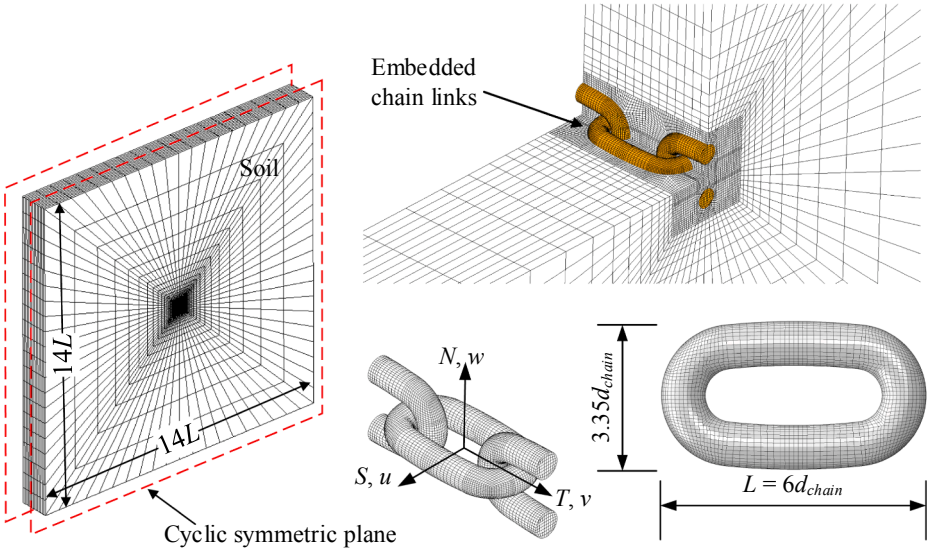

Fig. 12. Finite element model for chain link.

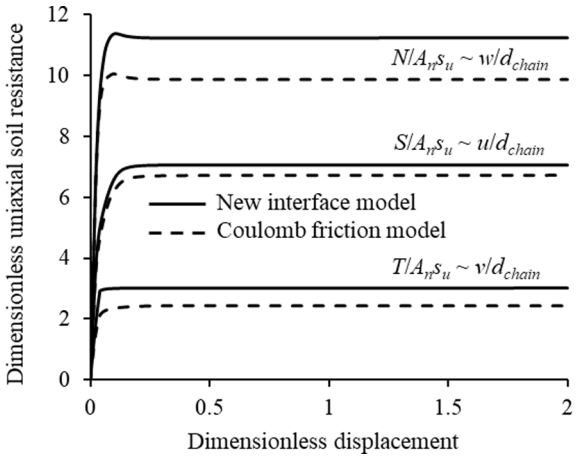

Fig. 13. Resistance response of chain link ($\alpha = 1$).

coupling the corresponding nodes on the front and back boundary faces. The bottom face of the soil was fixed, while two side faces of the soil were only allowed to have vertical displacement. The minimum size of soil elements close to the chain link was $0.05d_{chain}$, while a transition to coarse mesh was used further away from the chain. The soil model had approximately 140,000 hexahedral full integration elements.

Twelve different roughness, $\alpha = 0$, 0.2, 0.4, 0.6, 0.8, 1, 1.2, 1.4, 1.6, 1.8, 2 and 10^6 were considered. Also, a fully bonded interface was considered by using the 'Tie' constraint. For all the interfaces, three uniaxial soil resistances *T*, *N,* and *S* (along the axial, normal, and lateral directions) of the chain link were investigated. Thus, a total of $12 \times 2 \times 3 + 3 = 75$ analysis cases were conducted.

Fig. 13 shows the results of dimensionless factors $N_t = T/A_n s_u$, $N_n = N/A_n s_u$, and $N_s = S/A_n s_u$ for interface roughness $\alpha = 1$, where A_n is the normal project area of the chain link. The soil resistance increases with the displacement with a large stiffness, at first, and then reaches stabilised values, which are the uniaxial capacities. The results of the new interface model are larger than those of the Coulomb friction model, because the latter ignores friction on the trailing side when the normal force is in tension.

Fig. 14 summarises the capacity factors of all 75 calculation cases. For $\alpha = 0$ (the smooth interface), the capacity factors $N_{t\max} = 1.82$, $N_{n\max} = 8.45$ and $N_{s\max} = 6.00$ for both the new and Coulomb models. When $\alpha = 1$, the new interface model gives $N_{t\max} = 3.01$, $N_{n\max} = 11.25$, and $N_{s\max} = 7.04$. At $\alpha = 10^6$, the new interface model agrees with the

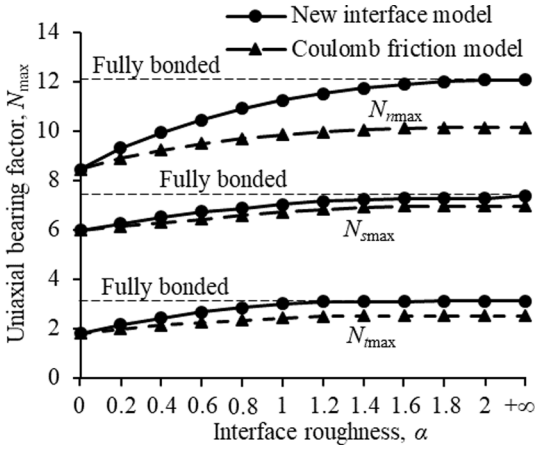

Fig. 14. Effect of interface roughness on uniaxial bearing factors of deeply embedded chain links.

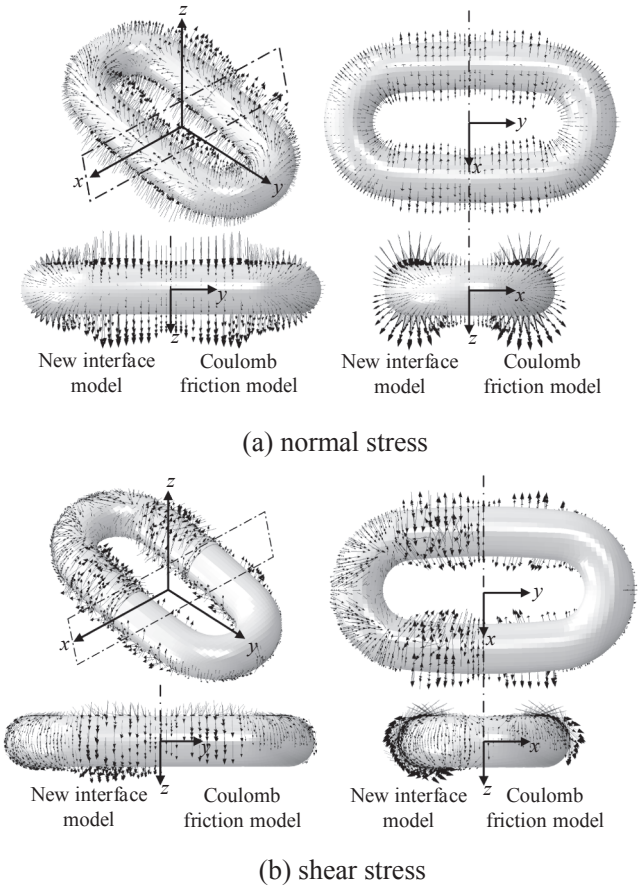

Fig. 15. Normal stress and shear stress of the deeply embedded chain link moving along the negative z-axis ($\alpha = 1$). (a) normal stress (b) shear stress.

fully bonded interface, where the bearing capacity factors are $N_{t\max} = 3.12$, $N_{n\max} = 12.08$, and $N_{s\max} = 7.28$, which increase by 3.89%, 6.87%, and 4.83%, respectively, compared with the cases of $\alpha = 1$. This clearly indicates that $\alpha = 1$ is not able to represent the fully bonded condition. The reason is that, for fully bonded conditions, relative sliding between the contact surfaces is not allowed, and thus, more shear failure occurs inside the soil. At $\alpha = 1$, the Coulomb friction model predicted $N_{t\max} = 2.44$, $N_{n\max} = 9.86$, and $N_{s\max} = 6.73$, which are 18.94%, 12.36%, and 4.40% smaller than the new interface model. The discrepancy of the two models increases with α up to 2 and then remains nearly constant afterwards.

The Coulomb friction model underpredicts the bearing capacity factors due to the lack of a friction on the trailing half of the chain link, which is in tension. The reason is explained in Fig. 15, which shows the shear stress distribution for the case of normal axial resistance (where the chain link was displaced along the *z*-axis) for $\alpha = 1$. This figure comprises two half link, where the left half is for the new interface model, while the right half is for the Coulomb friction model. It can be seen again that the Coulomb friction model predicts no friction on the trailing part of the chain link because the normal force on the trailing side is in tension. Again, the new interface model proposed in this note enables more appropriate undrained behaviour modelling, especially for interactions with complex geometries.

5. Conclusions

A new interface model was developed to enable undrained behaviour modelling of soil-structure interactions. It was implemented in finite element software ABAQUS by coding the user subroutine FRIC. The

tangential behaviour was defined based on the elastic-perfectly plastic constitutive relationship and an explicit integration algorithm was presented to facilitate numerical implementation. The new interface model has been validated and compared with the Coulomb friction model through three computational cases. The new interface model gives the same results as the fully bonded condition when a large α is used. The Coulomb friction model, on the other hand, underpredicts soil resistance because it gives zero tangential resistance when the normal stress is in tension. Therefore, the new interface model reported here is recommended to simulate undrained behaviour modelling where varying interface roughness needs to be considered.

CRediT authorship contribution statement

Wenlong Liu: Data curation, Formal analysis, Investigation, Methodology, Software, Validation, Writing – original draft. **Yinghui Tian:** Conceptualization, Funding acquisition, Methodology, Supervision, Visualization, Writing – review & editing, Resources. **Mark J. Cassidy:** Supervision, Writing – review & editing.

Declaration of Competing Interest

The authors declare that they have no known competing financial interests or personal relationships that could have appeared to influence the work reported in this paper.

Acknowledgements

This research was undertaken with support from the Australian Research Council (ARC) Discovery Project (DP190103315). The second author acknowledges the ARC Future Fellowship (FT200100457) for the support of conducting frontier research in offshore geotechnics.

References

ABS, 2017. Guide for the Certification of Offshore Mooring Chain. American Bureau of Shipping, Houston, p. 55.

Amaireh, L.K., Haikal, G., 2018. The stick-slip decomposition method for modeling large-deformation Coulomb frictional contact. Coupled Syst. Mech. 7 (5), 583–610. https://doi.org/10.12989/csm.2018.7.5.583.

Dassault Systèmes, 2014. ABAQUS Analysis User's Guide. Simulia Corp., Providence, RI.

DeJong, J.T., Yafrate, N.J., DeGroot, D.J., 2011. Evaluation of undrained shear strength using full-flow penetrometers. J. Geotech. Geoenviron. Eng. 137 (1), 14–26. https://doi.org/10.1061/(ASCE)GT.1943-5606.0000393.

Dingle, H.R.C., White, D.J., Gaudin, C., 2008. Mechanisms of pipe embedment and lateral breakout on soft clay. Can. Geotech. J. 45 (5), 636–652. https://doi.org/10.1139/T08-009.

DNVGL, 2015. Offshore Mooring Chain. DNVGL-OS-E302. DNV GL AS.

Gourvenec, S., Randolph, M.F., Kingsnorth, O., 2006. Undrained bearing capacity of square and rectangular footings. Int. J. Geomech. 6 (3), 147–157. https://doi.org/10.1061/(asce)1532-3641(2006)6:3(147).

Hodder, M., Cassidy, M.J., Barrett, D., 2008. In: Undrained Response of Shallow Pipelines Subjected to Combined Loading. IHS BRE Press, Bracknell, UK, pp. 897–908.

Hossain, M.S., Randolph, M.F., Hu, Y., White, D.J., 2006. Cavity stability and bearing capacity of Spudcan foundations on clay. In: Offshore Technology Conference. Houston, Texas, U.S.A.: Offshore Technology Conference, pp. 1–18. https://doi.org/10.4043/17770-ms.

Martin, C.M., Randolph, M.F., 2006. Upper-bound analysis of lateral pile capacity in cohesive soil. Geotechnique 56 (2), 141–145. https://doi.org/10.1680/geot.2006.56.2.141.

Merifield, R., White, D.J., Randolph, M.F., 2008. The ultimate undrained resistance of partially embedded pipelines. Géotechnique 58 (6), 461–470. https://doi.org/10.1680/geot.2007.00097.

Neubecker, S.R., Randolph, M.F., 1995. Profile and frictional capacity of embedded anchor chains. J. Geotech. Eng. 121 (11), 797–803. https://doi.org/10.1061/(ASCE)0733-9410(1995)121:11(797).

O'Neill, M.P., Bransby, M.F., Randolph, M.F., 2003. Drag anchor fluke-soil interaction in clays. Can. Geotech. J. 40 (1), 78–94. https://doi.org/10.1139/t02-096.

Qiu, G., Henke, S., Grabe, J., 2011. Application of a Coupled Eulerian-Lagrangian approach on geomechanical problems involving large deformations. Comput. Geotech. 38 (1), 30–39. https://doi.org/10.1016/j.compgeo.2010.09.002.

Randolph, M.F., Andersen, K.H., 2006. Numerical analysis of T-bar penetration in soft clay. Int. J. Geomech. 6 (6), 411–420.

Randolph, M.F., Houlsby, G.T., 1984. The limiting pressure on a circular pile loaded laterally in cohesive soil. Géotechnique 34 (4), 613–623.

Ramirez, R., Ahn, J., Kim, I., 2014. Effect of interaction characteristics on the holding capacity of suction caisson anchors. In: 2014 World Congress on Advances in Civil, Environmental, and Materials Research (ACEM14), Busan, Korea. Techno-Press, Daejeon, Korea, pp. 1–11.

Shen, Z., Feng, X., Gourvenec, S., 2016. Undrained capacity of surface foundations with zero-tension interface under planar V-H-M loading. Comput. Geotech. 73, 47–57. https://doi.org/10.1016/j.compgeo.2015.11.024.

Tian, Y., Cassidy, M.J., 2010. The challenge of numerically implementing numerous force-resultant models in the stability analysis of long on-bottom pipelines. Comput. Geotech. 37 (1–2), 216–232. https://doi.org/10.1016/j.compgeo.2009.09.004.

Wang, Y., Hu, Y., Hossain, M.S., 2017. End effect of T-bar penetrometer using 3D FE analysis. In: Proceedings of the Twenty-seventh (2017) International Ocean and Polar Engineering Conference, San Francisco, CA, USA. Cupertino, California, USA: The International Society of Offshore and Polar Engineers (ISOPE), vol. 45, pp. 725–732.

Yen, B.C., Tofani, G.D., 1984. Soil resistance to stud link chain. In: Offshore Technology Conference. Houston, Texas, U.S.A.: Offshore Technology Conference, pp. 479–488.

Zhou, H., Randolph, M.F., 2007. Computational techniques and shear band development for cylindrical and spherical penetrometers in strain-softening clay. Int. J. Geomech. 7 (4), 287–295.

Zhou, T., Tian, Y., Cassidy, M.J., 2018. Effect of tension on the combined loading failure envelope of a pipeline on soft clay seabed. Int. J. Geomech. 18 (10), 1–10. https://doi.org/10.1061/(ASCE)GM.1943-5622.0001246.